Article

Contourlet-based active contour model for PET image segmentation

ABDOLI, M, DIERCKX, R A J O, ZAIDI, Habib

Abstract

PET-guided radiation therapy treatment planning, clinical diagnosis, assessment of tumor growth, and therapy response rely on the accurate delineation of the tumor volume and quantification of tracer uptake. Most PET image segmentation techniques proposed thus far are suboptimal in the presence of heterogeneity of tracer uptake within the lesion. This work presents an active contour model approach based on the method of Chan and Vese ["Active contours without edges," IEEE Trans. Image Process. 10, 266-277 (2001)] designed to take into account the high level of statistical uncertainty (noise) and to handle the heterogeneity of tumor uptake typically present in PET images.

Reference

UNIVERSITÉ
DE GENÈVE

Contourlet-based active contour model for PET image segmentation

M. Abdoli and R. A. J. O. Dierckx
Department of Nuclear Medicine and Molecular Imaging, University of Groningen, University Medical Center Groningen, Groningen 9700 RB, The Netherlands

H. Zaidi[a)]
Division of Nuclear Medicine and Molecular Imaging, Geneva University Hospital, CH-1211 Geneva, Switzerland; Geneva Neuroscience Center, Geneva University, CH-1205 Geneva, Switzerland; and Department of Nuclear Medicine and Molecular Imaging, University of Groningen, University Medical Center Groningen, 9700 RB Groningen, The Netherlands

Purpose: PET-guided radiation therapy treatment planning, clinical diagnosis, assessment of tumor growth, and therapy response rely on the accurate delineation of the tumor volume and quantification of tracer uptake. Most PET image segmentation techniques proposed thus far are suboptimal in the presence of heterogeneity of tracer uptake within the lesion. This work presents an active contour model approach based on the method of Chan and Vese ["Active contours without edges," IEEE Trans. Image Process. **10**, 266–277 (2001)] designed to take into account the high level of statistical uncertainty (noise) and to handle the heterogeneity of tumor uptake typically present in PET images.
Methods: In the proposed method, the fitting terms in the Chan-Vese formulation are modified by introducing new input images, including the smoothed version of the original image using anisotropic diffusion filtering (ADF) and the contourlet transform of the image. The advantage of utilizing ADF for image smoothing is that it avoids blurring the object's edges and preserves the average activity within a region, which is important for accurate PET quantification. Moreover, incorporating the contourlet transform of the image into the fitting terms makes the energy functional more effective in directing the evolving curve toward the object boundaries due to the enhancement of the tumor-to-background ratio (TBR). The proper choice of the energy functional parameters has been formulated by making a clear consensus based on tumor heterogeneity and TBR levels. This cautious parameter selection leads to proper handling of heterogeneous lesions. The algorithm was evaluated using simulated phantom and clinical studies, where the ground truth and histology, respectively, were available for accurate quantitative analysis of the segmentation results. The proposed technique was also compared to a number of previously reported image segmentation techniques.
Results: The results were quantitatively analyzed using three evaluation metrics, including the spatial overlap index (SOI), the mean relative error (MRE), and the mean classification error (MCE). Although the performance of the proposed method was analogous to other methods for some datasets, overall the proposed algorithm outperforms all other techniques. In the largest clinical group comprising nine datasets, the proposed approach improved the SOI from 0.41 ± 0.14 obtained using the best-performing algorithm to 0.54 ± 0.12 and reduced the MRE from 54.23 ± 103.29 to 0.19 ± 16.63 and the MCE from 112.86 ± 69.07 to 60.58 ± 18.43.
Conclusions: The proposed segmentation technique is superior to other representative segmentation techniques in terms of highest overlap between the segmented volume and the ground truth/histology and minimum relative and classification errors. Therefore, the proposed active contour model can result in more accurate tumor volume delineation from PET images. © *2013 American Association of Physicists in Medicine*. [http://dx.doi.org/10.1118/1.4816296]

Key words: PET, segmentation, active contour, contourlet, anisotropic diffusion filter

1. INTRODUCTION

Accurate delineation of metabolically active regions of tumors is vital for PET-guided radiation therapy treatment planning, clinical diagnosis, tumor growth, and therapy response assessment.[1,2] The accurate definition of the tumor volume is especially important in radiation therapy, since underdosing may cause tumor recurrence and overdosing may lead to severe damage to the surrounding normal tissues.[3] However, segmentation of target volumes on PET images has re-

mained a challenging task for many years, due to the coarse spatial resolution and inherent noisy characteristics of PET images.[4,5]

Numerous PET image segmentation techniques have been proposed during the last few years, with manual delineation still being the most widely used method in the clinic. However, due to its vulnerability with respect to intra- and inter-observer variability and reproducibility, automated and semi-automated segmentation techniques have been promoted as alternative techniques and are generally preferred over the

manual technique. PET image segmentation techniques are generally categorized in four groups: thresholding techniques, variational approaches, learning methods, and stochastic modeling-based methods.[4] In a recent work, we selected representative methods from each category and compared their relative performance using clinical studies where the 3D contour derived on the macroscopic specimen was used as reference for comparison.[6] Five thresholding techniques, including a fixed percentage of the maximum standardized uptake value (SUV) (Ref. 7) and four adaptive thresholding methods,[8–11] one variational approach referred to as deformable active contour model,[12] two learning methods including fuzzy C-means (FCM) (Refs. 13 and 14), and an improved version of FCM (FCM-SW) (Ref. 15) as well as the expectation maximization method[16,17] belonging to the stochastic modeling category were included in this comparative study. It was shown that the FCM-SW approach outperforms the other selected techniques; however, the deformable active contour model also appeared as a potent segmentation technique, provided that appropriate improvements are applied to the method.

The classical active contour model, known as snake, was proposed by Kass et al.[18] where an initial contour around the target deforms and moves toward the desired object's edges. The deformation of the contour is handled by minimizing an energy functional in such a way that the set of local minima matches the desired features of the image. The energy functional consists of two set of terms, commonly known as internal and external energies. The internal energy guarantees the smoothness of the contour, whereas the external energy serves to force the contour to move toward the desired features of the image. The traditional snake deforms the contour based on the gradient information and, as such, its performance depends on the position of the initial contour, that is, the initial contour must be located close to the target so that the external energy is strong enough to push the contour toward the object boundaries. Moreover, this model cannot automatically handle the topologic changes of the curve.

Geometric active contour models capable of handling the topological changes were introduced later by Caselles et al.[19] This model utilizes the gradient information of the image to define an edge detector to stop the evolving curve at the object boundaries. The energy functional minimization procedure is carried out using the level set formulation.[12] The region-based active contour models, initially introduced by Mumford and Shah,[20] do not depend on the image gradient. The curve deforms based on global regional information of the image, which leads to outperformance of the model over classical approaches. The region-based active contour technique proposed by Chan and Vese[21] is a reduced form of the Mumford and Shah model, which proved to be efficient in the presence of discontinuities or blurriness across the boundaries.

In this work, an active contour model based on the work presented by Chan and Vese[21] is proposed for tumor volume delineation on PET images. The proposed model aims to handle the high noise characteristics and heterogeneity of tumor uptake to improve the capability of the energy functional in attracting the contour toward the object boundaries and to obtain a smooth surface over the segmented PET volume. We also provide a consensus regarding the choice of the parameters used in the energy functional in order to make the segmentation technique more robust.

2. MATERIALS AND METHODS

2.A. Proposed active contour model

We adopted the Chan-Vese (C-V) energy functional in our proposed active contour formulation owing to its potential to accurately delineate blurred edges.[21,22] The limited spatial resolution, partial volume effect, and high level of noise of PET images make the edge detection task a very challenging issue,[23,24] even for a potent region-based segmentation technique such as the C-V active contour method. In order to handle the intrinsic limitations of the energy functional formulation, we modified the fitting terms by introducing two input images. The original PET image, which serves as input to the C-V energy functional, is replaced by the smoothed image and the contourlet transform of the image. The regularizing terms have also been modified to keep the evolving surface as smooth as possible. To achieve this aim, the curvature of the evolving curve substituted the length and area of the curve. In Subsections 2.A.1–2.A.3, each modified term of the energy functional is explained separately.

2.A.1. Anisotropic diffusion filtering

The anisotropic diffusion filter (ADF) is the filter of choice to smooth low resolution blurred images due to its edge-enhancing and intraregional intensity-preserving features, which are crucial for accurate boundary delineation and quantification of PET data.[25] We have applied the ADF model proposed by Perona and Malik,[26] which is defined as follows:

$$\partial_t I = \mathrm{div}(g(|\nabla I|^2)\nabla I), \tag{1}$$

where I is the original image in gray scale, $\partial_t I$ is the partial derivative of I with respect to diffusion time t, and g is the diffusivity function defined as

$$g(|\nabla I|^2) = \frac{1}{1 + |\nabla I|^2/\lambda^2} \qquad (\lambda > 0), \tag{2}$$

where the constant λ is estimated using the noise estimator proposed by Canny.[27]

ADF is a suitable filtering technique for low count PET images which improve their qualitative aspects without impacting their quantitative characteristics. Figure 1(b) illustrates the efficient intraregion smoothing and edge-preserving characteristics of ADF. The smoothed version of the PET image is used as input to the proposed active contour model to enable more accurate delineation of the lesion contours.

2.A.2. Contourlet transform

The contourlet transform of the original image, which is utilized as second input to the fitting terms of the energy functional, provides a multiresolution and directional image expansion using contour segments. Do and Vetterli[28] introduced this transform as an efficient sparse representation of an
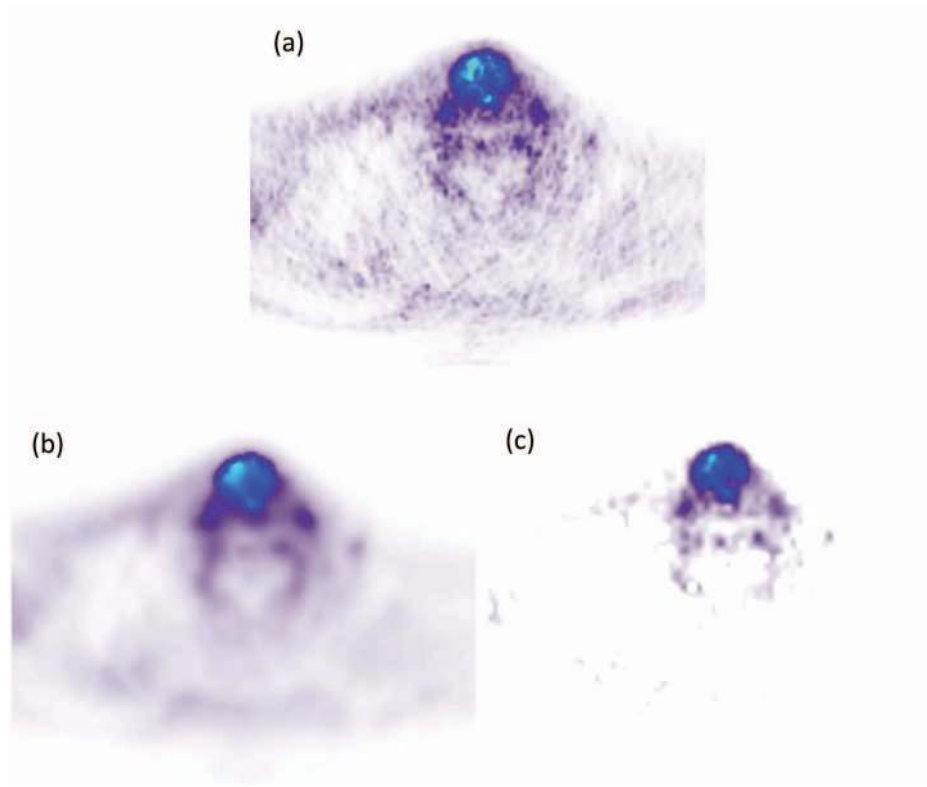
FIG. 1. Representative slice of a clinical PET study with laryngeal squamous cell carcinoma showing: (a) the original PET image, (b) the ADF smoothed image, and (c) the contourlet transform of the image.

image to capture significant features of the object of interest. The wavelet transform also provides an optimal representation for one-dimensional piecewise smooth signals,[29] but in two dimensions, where they are obtained by a tensor product of one-dimensional wavelets, they are only capable of isolating the discontinuities at edge points and fail to realize the smooth nature of the boundaries along the contours.[30]

The contourlet transform uses a wavelet-like transform to detect the discontinuous points on the edges, and then utilizes a local directional transform to link the captured points and detect the contour segments (contourlets). This is done by constructing a double filter bank structure, consisting of a Laplacian pyramid (LP) decomposition[31] followed by a directional filter bank (DFB) image decomposition[32] of each LP scale level. The contourlet transform generates 2^{l_j} high frequency images at each LP decomposition level j, where l_j is the number of DFB sub-bands. At each finer scale, the number of DFB decomposition levels is doubled and at the finest scale, there are five decomposition levels. Keeping the most significant contourlet coefficients results in improvement for many different applications of contourlet transforms, such as compression, denoising, and feature extraction. It must be

noted that the significant coefficients are produced by the contourlets which match both location and direction of the image contours.[28] Figure 2 represents a schematic illustration of the multiscale and directional decomposition using the contourlet transform. In our experiments, we have opted to truncate the contourlet coefficients to the 200 most significant ones and to reconstruct the image using the selected coefficients, which has resulted in an improved target-to-background ratio [Fig. 1(c)].

2.A.3. Curvature, the regularizing term

The curvature of a curve is used as a measure of the speed in changing direction at a given point. In order to prevent the evolving curve to get a fluctuating shape and to keep it as smooth as possible, we utilized the curvature of the curve as a fitting term in the energy functional. By minimizing the whole energy functional, the curvature will be in essence minimized, leading to a smooth surface over the segmented object.

In 3D, the curvature of a surface defined as a function of location, $f(x, y, z)$, is known as Gaussian curvature K,

$$K = \frac{\left(f_{xx}\left(f_y^2 + f_z^2\right) + f_{yy}\left(f_x^2 + f_z^2\right) + f_{zz}\left(f_x^2 + f_y^2\right) - 2f_{xy}f_xf_y - 2f_{xz}f_xf_z - 2f_{yz}f_yf_z\right)}{\left(f_x^2 + f_y^2 + f_z^2\right)^{3/2}},$$
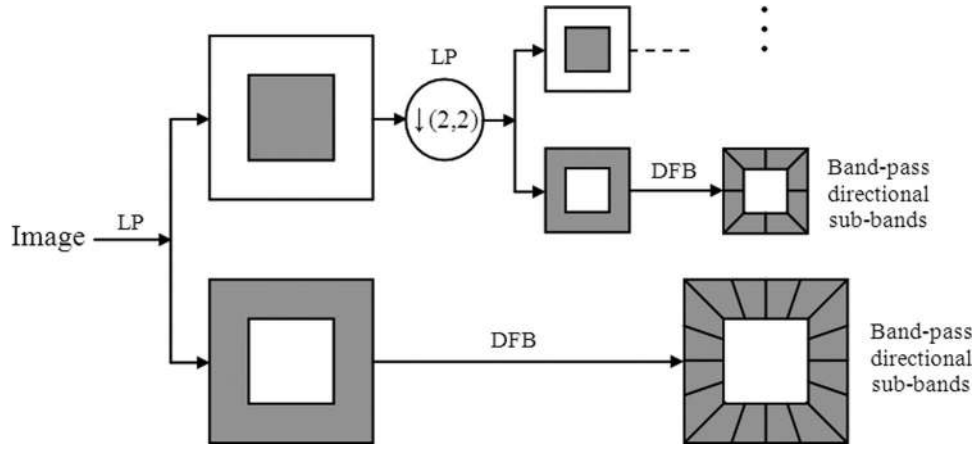
(3)

FIG. 2. Schematic illustration of the contourlet filter bank. LP stands for Laplacian pyramid and DFB stands for directional filter bank.

where $f_.$ and $f_{..}$ are the first and second partial derivatives of the curve with respect to the location (x, y, z).[12]

2.A.4. The energy functional formulation

Classical active contour models construct a stopping edge-function based on the gradient of the image $I(x, y)$. The stopping function might never reach zero since the discrete gradient is delimited, which might lead the evolving curve to get trapped in local minima states or makes it permeate through the boundary of the object. Unlike traditional active contour models, the C-V method[21] does not apply a stopping function and the evolving curve converges based on the Mumford and Shah formulation.[20] Chan and Vese[21] introduced the following energy functional:

$$E\left(c_{\mathrm{in}}, c_{\mathrm{out}}, C\right) = \mu.\mathrm{Length}\left(C\right) + \nu.\mathrm{Area}\left(\mathrm{inside}\left(C\right)\right)$$
$$+ \lambda_{\mathrm{in}} \int_{\mathrm{inside}(C)} |I\left(x, y\right) - c_{\mathrm{in}}|^2 dx\, dy$$
$$+ \lambda_{\mathrm{out}} \int_{\mathrm{outside}(C)} |I\left(x, y\right) - c_{\mathrm{out}}|^2 dx\, dy, \tag{4}$$

where the evolving curve in Ω is denoted as C and is defined as the boundary of an open subset of Ω, c_{in}, and c_{out} are the averages of the image $I(x, y)$ inside and outside C, respectively, and μ, ν, λ_{in}, and λ_{out} are positive constants. The first two terms of the functional, known as regularizing terms, measure the length and the area inside the curve, and the last two terms are the fitting terms.

In our proposed energy functional formulation, the C-V regularizing terms are modified to improve the smoothness of the evolving curve. The second term, which calculates the area inside the contour, has been set to zero in the original formulation by Chan and Vese,[21] and in our experiments, the first term appeared to be not effectively influencing the curve evolution process. Therefore, these two terms are replaced by a more effective regularizing term, which measures the curvature of the evolving curve, as explained in Subsection 2.A.3. The fitting terms are also modified by replacing the original

image by the smoothed version of the image (I^s) using ADF to handle the noisy characteristics of PET images. An extra input image is also introduced to the fitting terms to enhance the target/background contrast and to improve the edge detection feature of the algorithm. For this purpose, the contourlet transform of the image (I^c) is used as second input to the energy functional. The original 2D formulation of the energy functional has been properly extended to 3D in order to enable 3D segmentation of the lesion.

The energy functional proposed in this work is formulated as follows:

$$E\left(c_{\mathrm{in}}^s, c_{\mathrm{out}}^s, c_{\mathrm{in}}^c, c_{\mathrm{out}}^c, C\right)$$
$$= \mu.\mathrm{Curvature}\left(C\right) + \lambda_{\mathrm{in}} \int_{\mathrm{in}(C)} \left[\left|I^s(x, y, z) - c_{\mathrm{in}}^s\right|^2\right.$$
$$+ \left|I^c(x, y, z) - c_{\mathrm{in}}^c\right|^2\right] dx\, dy\, dz$$
$$+ \lambda_{\mathrm{out}} \int_{\mathrm{out}(C)} \left[\left|I^s(x, y, z) - c_{\mathrm{out}}^s\right|^2\right.$$
$$+ \left|I^c(x, y, z) - c_{\mathrm{out}}^c\right|^2\right] dx\, dy\, dz, \tag{5}$$

where c_{in}^s and c_{out}^s are the averages of I^s inside and outside the evolving curve C, respectively, c_{in}^c and c_{out}^c are the averages of I^c inside and outside the evolving curve, respectively, and μ, λ_{in}, and λ_{out} are user-defined positive constants.

The energy functional is minimized by means of the level set formulation.[12] The level set formulation represents the evolving curve by the zero level set of a Lipschitz function $\phi : \Omega \to \mathbb{R}$, in such a way that the function ϕ has a positive value inside and a negative value outside the curve. In the level set formulation the variable C is replaced by ϕ and, utilizing the Euler-Lagrange equation, the energy functional is minimized with respect to ϕ. Therefore, the terms in the energy functional are expressed in the level set formulation as follows:

$$\mathrm{Curvature}\left\{\phi = 0\right\} = \int_\Omega \mathrm{div}\left(\frac{\nabla\phi\left(x, y, z\right)}{|\nabla\phi\left(x, y, z\right)|}\right) dx\, dy\, dz, \tag{6}$$

$$\int_{\phi>0} \left[\left| I^s(x,y,z) - c_{\text{in}}^s \right|^2 + \left| I^c(x,y,z) - c_{\text{in}}^c \right|^2 \right] dx\, dy\, dz$$

$$= \int_{\Omega} \left[\left| I^s(x,y,z) - c_{\text{in}}^s \right|^2 + \left| I^c(x,y,z) - c_{\text{in}}^c \right|^2 \right]$$

$$\times H(\phi(x,y,z))\, dx\, dy\, dz,$$

$$\int_{\phi<0} \left[\left| I^s(x,y,z) - c_{\text{out}}^s \right|^2 + \left| I^c(x,y,z) - c_{\text{out}}^c \right|^2 \right] dx\, dy\, dz$$

$$= \int_{\Omega} \left[\left| I^s(x,y,z) - c_{\text{out}}^s \right|^2 + \left| I^c(x,y,z) - c_{\text{out}}^c \right|^2 \right]$$

$$\times (1 - H(\phi(x,y,z)))\, dx\, dy\, dz,$$

where H denotes the Heaviside function, defined as

$$H(u) = \begin{cases} 1 & \text{if } u \geq 0 \\ 0 & \text{if } u < 0 \end{cases}.$$

The energy functional can now be written as follows:

$$E\left(c_{\text{in}}^s, c_{\text{out}}^s, c_{\text{in}}^c, c_{\text{out}}^c, \phi\right)$$

$$= \mu \int_{\Omega} \text{div}\left(\frac{\nabla \phi(x,y,z)}{|\nabla \phi(x,y,z)|} \right) dx\, dy\, dz$$

$$+ \lambda_{\text{in}} \int_{\Omega} \left[\left| I^s(x,y,z) - c_{\text{in}}^s \right|^2 + \left| I^c(x,y,z) - c_{\text{in}}^c \right|^2 \right]$$

$$\times H(\phi(x,y,z))\, dx\, dy\, dz$$

$$+ \lambda_{\text{out}} \int_{\Omega} \left[\left| I^s(x,y,z) - c_{\text{out}}^s \right|^2 + \left| I^c(x,y,z) \right. \right.$$

$$\left. \left. - c_{\text{out}}^c \right|^2 \right] (1 - H(\phi(x,y,z)))\, dx\, dy\, dz. \tag{7}$$

To minimize the energy functional E with respect to ϕ, the Euler-Lagrange equation is used. For this purpose, a dummy time parameter $t \geq 0$ is introduced to the level set function $\phi(t,x,y,z)$ and the Euler-Lagrange equation is written as

$$\frac{\partial \phi}{\partial t} = \mu \left| \nabla \left(\text{div}\left(\frac{\nabla \phi}{|\nabla \phi|} \right) \right) \right| - \delta(\phi) \left[\lambda_{\text{in}} \left(\left(I^s - c_{\text{in}}^s \right)^2 \right. \right.$$

$$\left. \left. + \left(I^c - c_{\text{in}}^c \right)^2 \right) - \lambda_{\text{out}} \left(\left(I^s - c_{\text{out}}^s \right)^2 + \left(I^c - c_{\text{out}}^c \right)^2 \right) \right] = 0, \tag{8}$$

where $\phi(0,x,y,z) = \phi_0(x,y,z)$ defines the initial contour and $\delta(\phi)$ is the Dirac delta function, defined as the derivative of the Heaviside function with respect to ϕ.

We have used the following numerical approximation of the Heaviside function in our formulation:[33]

$$H_\varepsilon(x) = \begin{cases} 1 & \text{if } x > \varepsilon \\ 0 & \text{if } x < -\varepsilon \\ \frac{1}{2}\left[1 + \frac{x}{\varepsilon} + \frac{1}{\pi} \sin\left(\frac{\pi x}{\varepsilon} \right) \right] & \text{if } |x| \leq \varepsilon. \end{cases} \tag{9}$$

2.A.5. Parameter optimization

As mentioned earlier, the parameters μ, λ_{in}, and λ_{out} are determined by the user. The proper choice of the parameters

is of utmost importance since it can considerably alter the segmentation results. *A priori* knowledge of the factors influencing the performance of the algorithm can lead to better understanding of how the selection of the parameters should be done. It is also essential to recognize the role each parameter plays during the evolution procedure. The parameter μ is mainly responsible for normalization of the regularizing term so that its value is within the range of fitting terms. For this purpose, we have experimentally defined an adaptive formulation which calculates the proper value of the parameter μ,

$$\mu = 15.\max\left\{ \left(I^s - c_{\text{out}}^s \right)^2, \left(I^c - c_{\text{out}}^c \right)^2 \right\}. \tag{10}$$

The parameter λ_{in} decides how strongly the internal energy attracts the contour inwards. Therefore, in cases of low tumor-to-background ratios (TBRs), a higher value of λ_{in} is required to attract the contour toward the low-contrast edges. In contrast, λ_{out} modulates the strength of the external energy moving the contour outwards. In cases of high heterogeneity in the lesion uptake, a higher value of λ_{out} is required in order to force the contour toward the boundaries of the lesion.

To get a clear insight into the behavior of the algorithm when λ_{in} and λ_{out} are modified, we have examined the segmentation results by setting one of these parameters to 1 and altering the other successively within the range $[1\ldots 10]$. Plotting the segmented volume over the parameter values illustrates appropriately how the algorithm behaves when the parameters are modified and guides the user to select the best combination of the parameters under various TBR and heterogeneity conditions.

2.B. Phantom and clinical studies

The performance evaluation of the proposed segmentation technique was performed using a simulated phantom study by means of the 4D extended cardio-torso (XCAT) phantom.[34] The phantom was originally designed to allow the user to simulate spherical lesions with homogeneous activity concentration, which does not emulate realistically clinical situations. As such, we followed the procedure proposed by Le Maitre *et al.*[35] to simulate an irregular shaped tumor with heterogeneous activity concentration. This realistic tumor simulation consists of the following steps. First, the tumors are manually segmented from a clinical PET dataset and a 3D mesh is constructed over the whole volume using the AMIRA software (http://www.vsg3d.com/amira). Thereafter, since the organs in the XCAT phantom are modeled using nonuniform rational B-spline (NURBS) surfaces, the generated 3D mesh is converted to a NURBS surface using Rhinoceros software (CADLINK, France). The heterogeneity within the tumor is modeled by defining NURBS surfaces of different sizes to which different activity levels are assigned. In our simulation, we have modeled two levels of activity concentration, which was reported to be sufficient for proper modeling of tumors with heterogeneous activity uptake.[35] For data simulation, we applied an analytical simulator incorporated within the Software for Tomographic Image Reconstruction (STIR) package.[36]

The proposed technique was further evaluated using various clinical databases of oncologic FDG-PET images including three head and neck datasets with T3-T4 laryngeal squamous cell carcinoma (Louvain database),[37] nine datasets of patients with lung tumors,[38] and two datasets of patients with head and neck cancer (University of Turku, Finland).[39] For all clinical datasets, except the last group, the 3D contours of the lesions, defined from the histology macroscopic specimen following surgical removal of the tumors, served as reference for evaluation. For the last group of clinical datasets, multiple expert delineations combined with statistical methods (inverse receiver operating characteristic approach) were used to provide a surrogate of the truth.[39] Four patients from the Louvain laryngeal carcinoma datasets and one patient from the Louvain lung datasets were discarded from the study owing to unexplained significant mismatch between the hot metabolic activity seen on PET images and the histology contours as reported by the Task Group No. 211 of the American Association of Physics in Medicine (AAPM).[40]

2.C. Comparative study and evaluation metrics

The proposed segmentation technique was compared with three other segmentation methods, including an adaptive thresholding proposed by Nestle et al.,[10] where the threshold is determined based on the mean intensity within the target and the surrounding background, the fuzzy clustering-based approach (FCM),[41] and its improved version referred to as FCM-SW, which incorporates spatial information to optimize the objective function with knowledge about spatial constraint and also handles the heterogeneous lesion uptake using the à trous wavelet transform of the image.[15]

To validate the proposed algorithm and compare its performance to the above referenced techniques, we used various metrics including the mean relative error (MRE) and the spatial overlap index (SOI), as well as the mean classification error (MCE) between the estimated and reference volumes,

$$\text{MRE} = \text{mean}\left(\frac{V_{\text{segmented}} - V_{\text{true}}}{V_{\text{true}}}\right) \times 100\%,$$

$$\text{SOI} = \frac{2(V_{\text{true}} \cap V_{\text{segmented}})}{(V_{\text{true}} + V_{\text{segmented}})},$$

$$\text{MCE} = \frac{(\text{PCE} + \text{NCE})}{\text{VoV}_{\text{true}}} \times 100\%, \tag{11}$$

where V_{true} is the true volume belonging to the ground truth/histology, $V_{\text{segmented}}$ is the segmented volume obtained using the different techniques, PCE and NCE are the positive and negative classification errors, respectively, and VoV_{true}
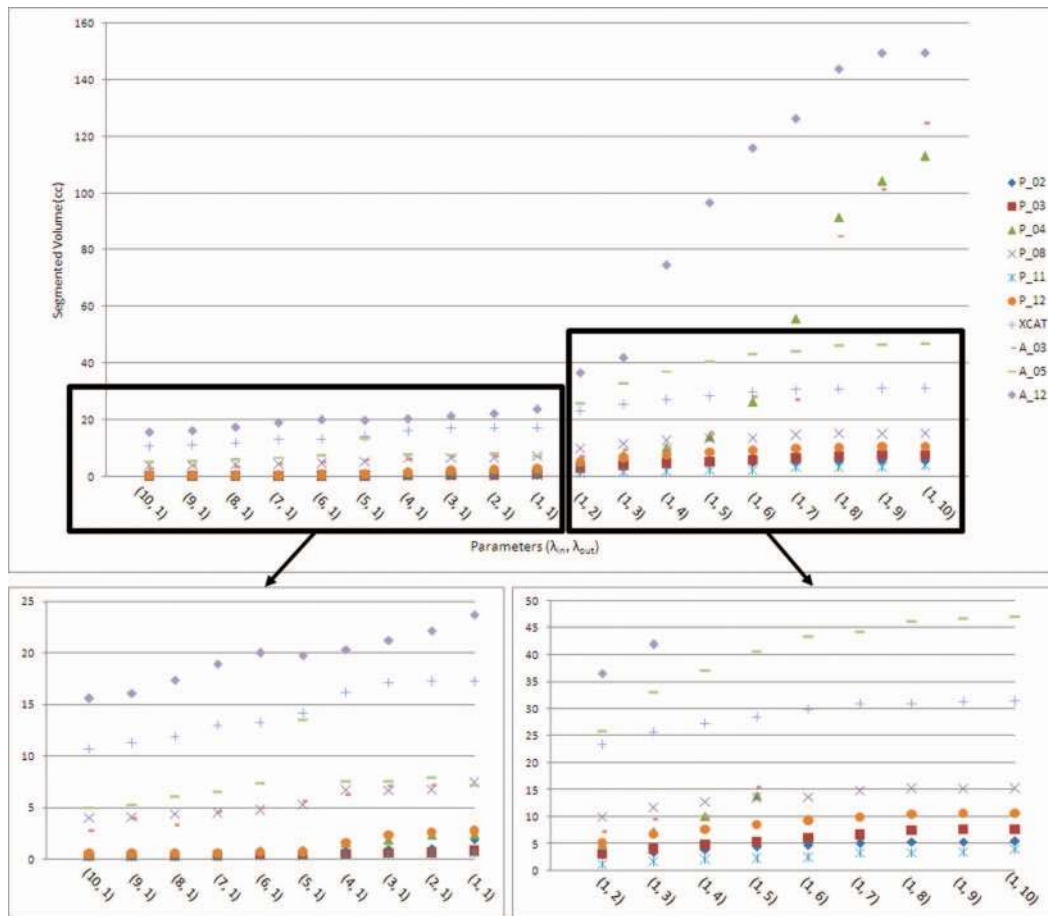

FIG. 3. Segmented volumes (in cc) for various combinations of the parameters (λ_{in}, λ_{out}). In the figure caption, P_n stands for the ID of the patient in the Louvain lung dataset, A_n stands for the ID of the patient in the Louvain pharyngolaryngeal carcinoma dataset.
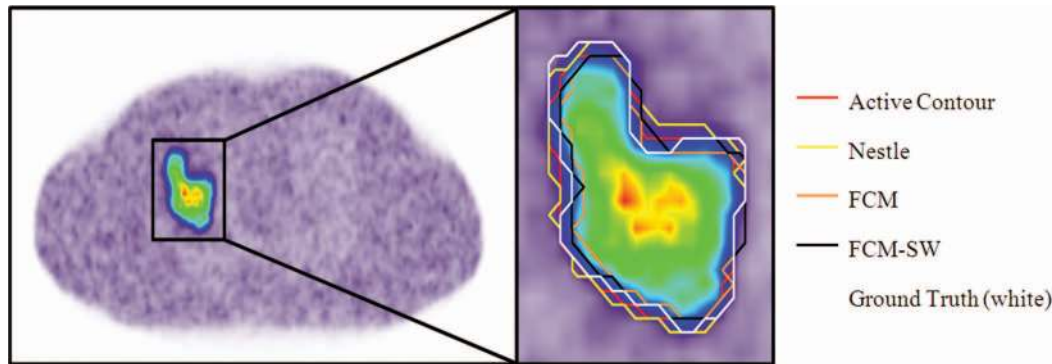
FIG. 4. Realistic irregularly shaped simulated lesion defined on the XCAT phantom with heterogeneous uptake together with the results using the proposed and commonly used PET image segmentation techniques as compared to the ground truth.

is the number of voxels within the ground truth volume.[42] The value of SOI varies between 0 and 1, where 0 corresponds to no overlap between the segmented volume and the ground truth and 1 characterizes full overlap between the two volumes.

3. RESULTS

As mentioned earlier, to optimize the parameters λ_{in} and λ_{out} in the energy functional, the performance of the algorithm was experimentally examined by altering one parameter in the range $[1\ldots10]$ and setting the other parameter to 1. The optimization procedure was performed on ten selected datasets, which showed better agreement between the ground truth and the visually observed high activity concentration on PET images. Figure 3 presents the results of this examination by plotting the segmented volume in cubic centimeters (cc) versus different combinations of the two parameters. Since the graphs show dissimilar trends in each half of the plot, each region is presented separately in a subplot below the main plot. On the right side of the subplot, the data points from the three datasets with exceedingly increasing values are eliminated for clear observation of the trend in other cases. The strange behavior of these three datasets is understandable as discussed in Sec. 4.

Both subplots shown in Fig. 3 show an approximately linear correlation between the segmented volume and successive alteration of the parameters. However, the slopes of the estimated lines are different. In general, setting λ_{in} to 1 and λ_{out} to a higher value results in a larger segmented volume. This was already expected due to the fact that λ_{out} forces the evolving curve to move outwards and, thus, a higher value of λ_{out} leads to stronger external energy that results in a larger segmented volume. On the other hand, setting λ_{out} to 1 and increasing the value of λ_{in} makes the internal energy stronger which pushes the evolving curve to move inwards and makes the segmented volume smaller.

Based on the ground truth volumes, it was observed that for cases with high TBRs a higher value of λ_{out} is required to obtain a segmented volume which is in close agreement with the true volume. In contrast, those cases presenting with

low TBR entail a higher λ_{in} value to reach an acceptable concordance. In the presence of high heterogeneity level in the tracer uptake, λ_{in} is set to 1 and a larger value has to be assigned to λ_{out}, whereas low heterogeneity levels require a high λ_{in} value and λ_{out} is set to 1. In our experiments λ_{in} varies within the range $[1\ldots3]$, and λ_{out} within the range of $[1\ldots6]$, depending on the TBR and the heterogeneity level.

The proposed segmentation technique and the three other methods were applied to the simulated heterogeneous lesion within the XCAT phantom. Figure 4 shows the obtained contours as well as the true contour of the simulated tumor. The quantitative analysis of the results is performed using the previously introduced evaluation metrics. Table I summarizes the segmentation results using the proposed as well as Nestle, FCM, and FCM-SW techniques.

Figure 5 illustrates the segmentation results on a representative slice from the Louvain laryngeal squamous cell carcinoma dataset. The ground truth contour is shown in white, whereas the contours generated by the PET image segmentation techniques are presented in different colors. It can be observed that the proposed and the FCM-SW methods can properly handle the heterogeneity of the lesion uptake. The results of the quantitative analysis of this dataset are presented in Fig. 6, where the segmented volumes are compared to the volume defined on the macroscopic specimen. It can be seen that FCM-SW and the proposed active contour method outperform similarly the other techniques. Although FCM-SW

TABLE I. Quantitative analysis of segmentation results of the realistic tumor simulated using the XCAT phantom obtained using the proposed and commonly used PET image segmentation techniques.

Segmentation method	Mean volume (cc)	SOI[a]	RE[a] (%)	CE[a] (%)
Nestle	35.51	0.80	19.11	24.63
FCM	23.45	0.76	−21.33	23.70
FCM-SW	27.29	0.83	−8.44	16.99
Active contour	29.94	0.85	0.44	16.18
True volume	29.81	…	…	…

[a]SOI = Spatial overlap index, RE = Relative error, CE = Classification error.
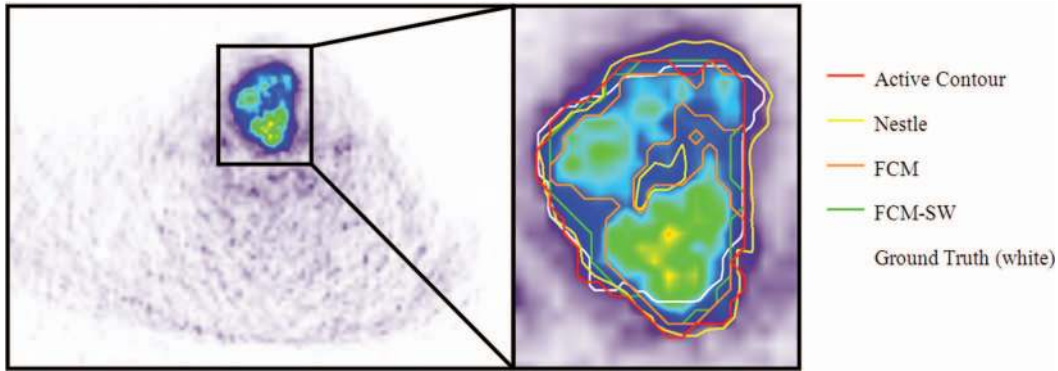
FIG. 5. Representative clinical PET study from the Louvain pharyngolaryngeal carcinoma dataset and comparison of the results obtained using the proposed and commonly used PET image segmentation techniques with the histology.

achieves slightly lower mean classification error and spatial overlap index, it must be emphasized that the mean relative error associated with FCM-SW is much higher compared to the proposed active contour model.

The segmentation results of the clinical lung datasets are presented in Fig. 7. The evaluation metrics used for the quantitative analysis are plotted in Fig. 8. It can be observed that our proposed method outperforms noticeably the other techniques for this group of datasets, which is the largest group used in this study. It must be noted that the large error bars in Figs. 6(a) and 8(a) are due to the large variation between lesion sizes and should not be misinterpreted as intrinsic bias induced by segmentation techniques.

Figure 9 represents an example of one clinical study belonging to the head and neck Turku datasets where the contours determined by the segmentation algorithms and the contour defined using the multiple expert delineation approach are shown. Due to the small sample size in this group (only two patients), we did not perform descriptive statistical analysis. Instead, all the evaluation metrics are reported in Table II. It can be seen that in the case of the large lesion (tumor "a"), Nestle's method performs very well, whereas the evaluation metrics are comparable to those of the active contour model. However, for the small lesion (tumor "b"), the proposed model outperforms significantly the other segmentation techniques.
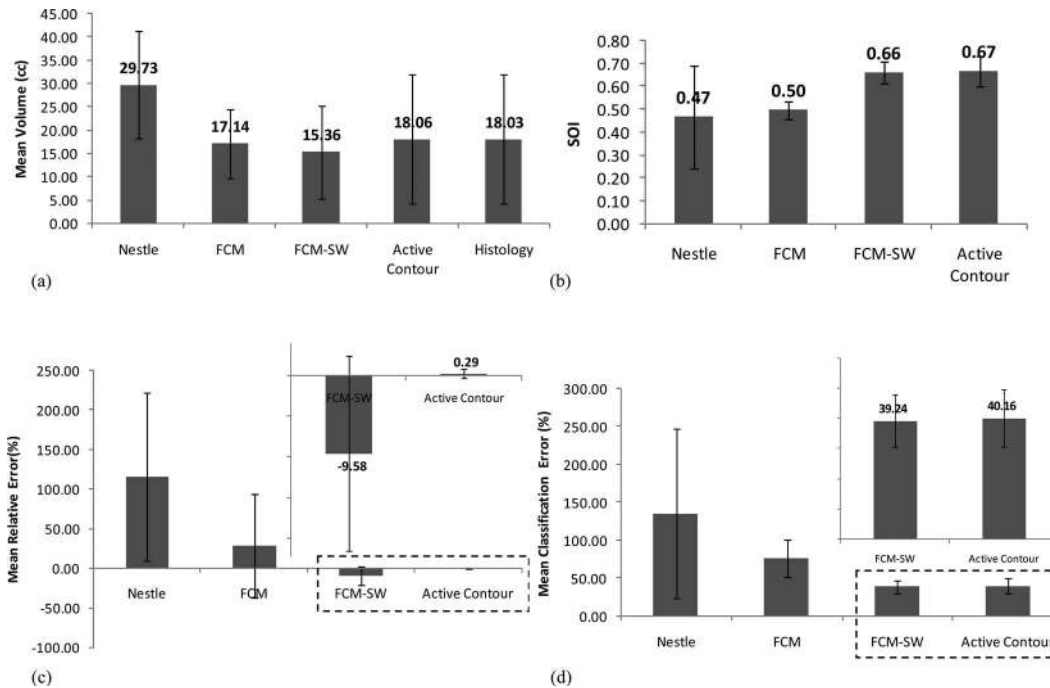

FIG. 6. Comparison between segmentation results obtained using the proposed and commonly used PET image segmentation techniques using the Louvain pharyngolaryngeal carcinoma datasets with histology: (a) mean volumes, (b) spatial overlap index, (c) mean relative error (%), and (d) mean classification error (%).
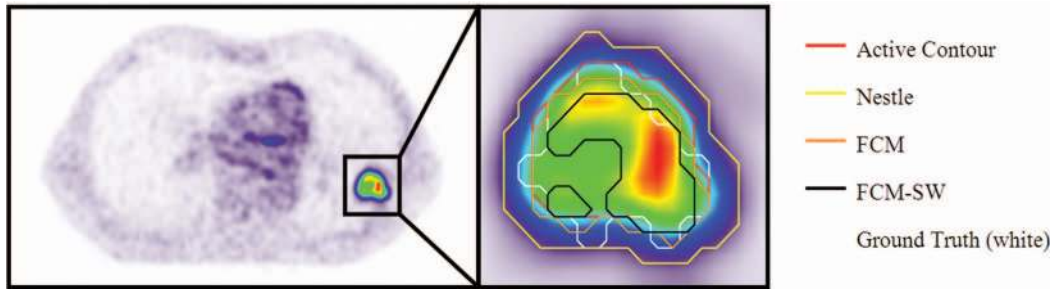
FIG. 7. Representative clinical PET image from the three Louvain lung dataset and comparison of the results obtained using commonly used PET image segmentation techniques with the histology.
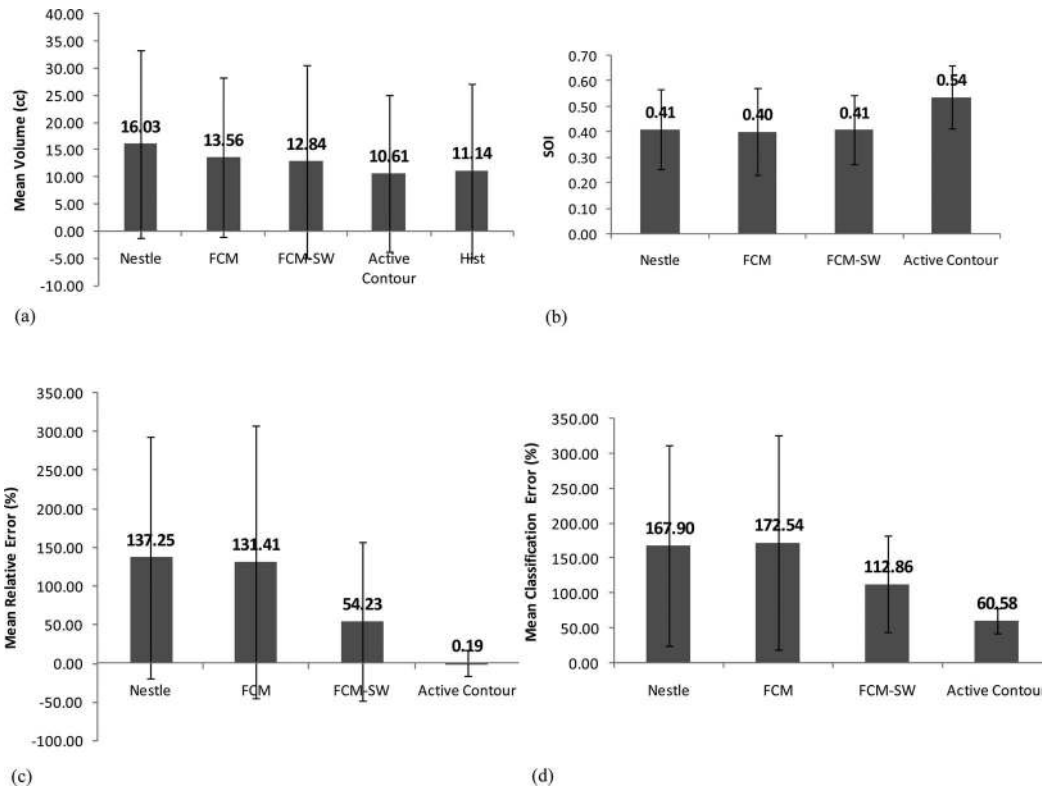

FIG. 8. Quantitative analysis of segmentation results of the nine Louvain clinical lung datasets obtained using the proposed and commonly used PET image segmentation techniques compared with the histology: (a) mean volumes, (b) spatial overlap index, (c) mean relative error (%), and (d) mean classification error (%).
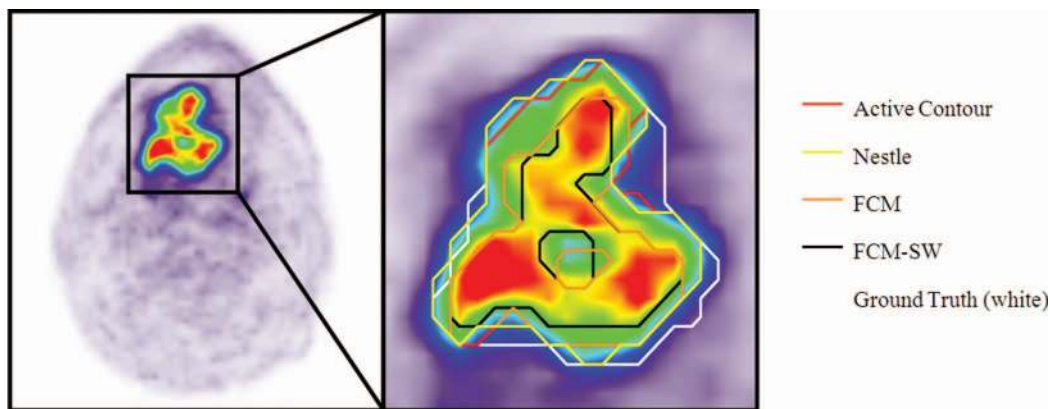

FIG. 9. Representative clinical PET image from Turku head and neck dataset and comparison of the results obtained using the proposed method and commonly used PET image segmentation techniques with the histology.

TABLE II. Quantitative analysis of segmentation results of the clinical head and neck datasets obtained using the proposed and commonly used PET image segmentation techniques. Tumor (a) indicates the dataset presenting with the large lesion whereas tumor (b) represents the dataset with the small lesion.

Segmentation method	Tumor volume (cc)		SOI[a]		RE[a] (%)		CE[a] (%)	
	Tumor a	Tumor b	Tumor a	Tumor b	Tumor a	Tumor b	Tumor a	Tumor b
Nestle	29.46	5.75	0.76	0.19	− 0.41	400.00	27.69	412.77
FCM	19.17	1.32	0.60	0.53	− 35.19	14.78	41.16	65.96
FCM-SW	19.36	1.56	0.60	0.57	− 34.55	35.65	41.82	65.96
Active contour	30.78	1.22	0.76	0.57	4.06	6.09	27.36	57.45
True volume	29.58	1.15	…	…	…	…	…	…

[a]SOI = Spatial overlap index, RE = Relative Error, CE = Classification error.

4. DISCUSSION

This work presents a deformable active contour model for PET tumor volume delineation, which handles appropriately the intrinsic high noise level of PET images and the heterogeneity of the tumor uptake by incorporating prior knowledge regarding the TBR and tumor heterogeneity. It also attempts to preserve the evolving curve as smooth as possible during the contour deformation by minimizing the curvature of the contour. Application of ADF, which is capable of preserving the object's edges and the mean intensity within the object volume, makes the handling of the high level of noise in PET images feasible without influencing PET quantification. Moreover, integrating the contourlet transform of the image to the energy functional formulation makes the fitting terms more potent in attracting the evolving curve toward the object boundaries due to the enhancement of the TBR.

The proper setting of the parameters λ_{in} and λ_{out} can influence the segmentation results significantly. Therefore, as mentioned in Sec. 1, we attempted to derive a clear and precise consensus of the choice of the parameters. For this purpose, the algorithm was examined by varying the values of one parameter in the range of $[1 \ldots 10]$, keeping the other parameter values fixed to 1. As can be seen in Fig. 3, the algorithm presents an approximately bilinear behavior. On the left subplot, λ_{out} is set to 1 and λ_{in} is decreasingly altered from 10 to 1. The segmented volume increases linearly with a small slope. A decrease in the values of λ_{in} is equivalent to reducing the power to push the contour inward, meaning that the evolving curve would stop at the borders of a larger volume. The right side subplot follows a similar trend, except that the linear behavior changes with a higher slope. By setting λ_{in} to 1 and increasing the value of λ_{out} from 2 to 10, the contour is forced outwards more strongly. In particular, in cases of low TBRs, an increase in the value of λ_{out} may cause an extraordinary increase of the segmented volume, which is the case for P_04, A_03, and A_12. This is why we have removed those data points on the right side subplot to present the behavior of other datasets more clearly. These results imply that in the case of low TBR, the parameter values must be selected based on the heterogeneity level of the tumor, either from the left side subplot, or λ_{in} must be set to 1 and the value of λ_{out} should not be far from that of λ_{in} to prevent the contour to exceedingly overestimate the volume.

Comparing the segmented volumes with the corresponding ground truth reveals that in the presence of high heterogeneity level in the tracer uptake, a λ_{in} equal to one and λ_{out} equal to or higher than one is required to stop the evolving curve at the right boundary of the object. A higher λ_{out} guarantees the sufficient strength of the external energy to push the contour away from the higher activity foci within the lesion and to move it out toward the correct boundaries of the target. However, when tumor heterogeneity is not pronounced, there is no need for stronger external energy and λ_{out} can conveniently be set to one and a higher value has to be assigned to λ_{in}, depending on the TBR level. The cautious selection of the parameters facilitates proper handling of the heterogeneity in tumor uptake.

The TBR level also has a vital role in the selection of parameters. In the presence of high TBR, a high λ_{out} value is required to stop the evolving curve at the right boundary of the object. This is due to the fact that a high TBR makes the internal energy stronger to attract the contour inwards and, as such, more powerful external energy is needed to avoid an underestimated segmented volume. However, in the case of low TBR, a higher λ_{in} is needed to force the contour to move toward the object's boundary.

The proposed algorithm is compared to three representative PET image segmentation techniques selected from a recent comparative study,[6] particularly those which were shown to outperform commonly used techniques. The quantitative analysis of the various segmentation approaches using phantom and clinical studies revealed that the proposed segmentation technique is superior to the representative methods. The accuracy of the techniques was tested using three evaluation metrics and all of them confirm the superiority of the proposed active contour model. The results demonstrate that among all the tested techniques, the proposed approach achieves the highest overlap between the segmented volume and the ground truth and the lowest mean relative and classification errors. However, in some few cases, the method proposed by Nestle and the FCM-SW technique competes with our method, but ultimately yield comparable results.

The visual assessment of the contours confirms that the algorithm successfully achieves a smooth contour over the segmented volume, which is not normally the case of classical active contour models when the image contains a high level of noise.

5. CONCLUSION

We have presented a deformable active contour model based on the method proposed by Chan and Vese.[21] A consensus was made to choose appropriate parameters for the energy functional to enable the model to handle heterogeneous tumors properly. We have also introduced new inputs to the energy functional to deal with the high levels of noise in PET images and to enhance the edge detection properties of the model. Incorporating the curvature of the evolving curve facilitates achieving a smooth contour over the segmented volume. The evaluation metrics used to quantitatively analyze phantom and clinical studies revealed the superiority of the proposed method over commonly used techniques, since it presents the highest overlap between the segmented volume and the corresponding ground truth and the lowest mean relative and classification errors. Therefore, the proposed active contour model results in more accurate tumor volume delineation from PET images.

a)Author to whom correspondence should be addressed. Electronic mail: habib.zaidi@hcuge.ch; Telephone: +41 22 372 7258; Fax: +41 22 372 7169.

[1] I. F. Ciernik, E. Dizendorf, B. G. Baumert, B. Reiner, C. Burger, J. B. Davis, U. M. Lutolf, H. C. Steinert, and G. K. Von Schulthess, "Radiation treatment planning with an integrated positron emission and computer tomography (PET/CT): A feasibility study," Int. J. Radiat. Oncol., Biol., Phys. **57**, 853–863 (2003).

[2] E. C. Ford, J. Herman, E. Yorke, and R. L. Wahl, "18F-FDG PET/CT for image-guided and intensity-modulated radiotherapy," J. Nucl. Med. **50**, 1655–1665 (2009).

[3] C. A. Perez, Principles and Practice of Radiation Oncology, 4th ed. (Lippincott Williams and Wilkins, Philadelphia, PA, 2004).

[4] H. Zaidi and I. El Naqa, "PET-guided delineation of radiation therapy treatment volumes: A survey of image segmentation techniques," Eur. J. Nucl. Med. Mol. Imaging **37**, 2165–2187 (2010).

[5] R. J. McGurk, J. Bowsher, J. A. Lee, and S. K. Das, "Combining multiple FDG-PET radiotherapy target segmentation methods to reduce the effect of variable performance of individual segmentation methods," Med. Phys. **40**, 042501 (9pp.) (2013).

[6] H. Zaidi, M. Abdoli, C. Fuentes, and I. El Naqa, "Comparative methods for PET image segmentation in pharyngolaryngeal squamous cell carcinoma," Eur. J. Nucl. Med. Mol. Imaging **39**, 881–891 (2012).

[7] Y. E. Erdi, O. Mawlawi, S. M. Larson, M. Imbriaco, H. Yeung, R. Finn, and J. L. Humm, "Segmentation of lung lesion volume by adaptive positron emission tomography image thresholding," Cancer **80**, 2505–2509 (1997).

[8] K. J. Biehl, F. M. Kong, F. Dehdashti, J. Y. Jin, S. Mutic, I. El Naqa, B. A. Siegel, and J. D. Bradley, "18F-FDG PET definition of gross tumor volume for radiotherapy of non-small cell lung cancer: Is a single standardized uptake value threshold approach appropriate?," J. Nucl. Med. **47**, 1808–1812 (2006).

[9] Q. C. Black, I. S. Grills, L. L. Kestin, C. Y. Wong, J. W. Wong, A. A. Martinez, and D. Yan, "Defining a radiotherapy target with positron emission tomography," Int. J. Radiat. Oncol., Biol., Phys. **60**, 1272–1282 (2004).

[10] U. Nestle, S. Kremp, A. Schaefer-Schuler, C. Sebastian-Welsch, D. Hellwig, C. Rube, and C. M. Kirsch, "Comparison of different methods for delineation of 18F-FDG PET-positive tissue for target volume definition in radiotherapy of patients with non-Small cell lung cancer," J. Nucl. Med. **46**, 1342–1348 (2005).

[11] A. Schaefer, S. Kremp, D. Hellwig, C. Rübe, C.-M. Kirsch, and U. Nestle, "A contrast-oriented algorithm for FDG-PET-based delineation of tumour volumes for the radiotherapy of lung cancer: Derivation from phantom measurements and validation in patient data," Eur. J. Nucl. Med. Mol. Imaging **35**, 1989–1999 (2008).

[12] S. Osher and J. A. Sethian, "Fronts propagating with curvature-dependent speed: Algorithms based on Hamilton-Jacobi formulations," J. Comput. Phys. **79**, 12–49 (1988).

[13] L. O. Hall, A. M. Bensaid, L. P. Clarke, R. P. Velthuizen, M. S. Silbiger, and J. C. Bezdek, "A comparison of neural network and fuzzy clustering techniques in segmenting magnetic resonance images of the brain," IEEE Trans. Neural Netw. **3**, 672–682 (1992).

[14] D. L. Pham and J. L. Prince, "An adaptive fuzzy C-means algorithm for image segmentation in the presence of intensity inhomogeneities," Pattern Recog. Lett. **20**, 57–68 (1999).

[15] S. Belhassen and H. Zaidi, "A novel fuzzy C-means algorithm for unsupervised heterogeneous tumor quantification in PET," Med. Phys. **37**, 1309–1324 (2010).

[16] K. Van Leemput, F. Maes, D. Vandermeulen, and P. Suetens, "Automated model-based tissue classification of MR images of the brain," IEEE Trans. Med. Imaging **18**, 897–908 (1999).

[17] J. Ashburner and K. J. Friston, "Unified segmentation," Neuroimage **26**, 839–851 (2005).

[18] M. Kass, A. Witkin, and D. Terzopoulos, "Snakes: Active contour models," Int. J. Comput. Vis. **1**, 321–331 (1988).

[19] V. Caselles, F. Catte, T. Coll, and F. Dibos, "A geometric model for active contours in image processing," Numer. Math. **66**, 1–31 (1993).

[20] D. Mumford and J. Shah, "Optimal approximations by piecewise smooth functions and associated variational problems," Commun. Pure Appl. Math. **42**, 577–685 (1989).

[21] T. F. Chan and L. A. Vese, "Active contours without edges," IEEE Trans. Image Process. **10**, 266–277 (2001).

[22] K. Khamwan, A. Krisanachinda, and C. Pluempitiwiriyawej, "Automated tumour boundary delineation on (18)F-FDG PET images using active contour coupled with shifted-optimal thresholding method," Phys. Med. Biol. **57**, 5995–6005 (2012).

[23] J. A. van Dalen, A. L. Hoffmann, V. Dicken, W. V. Vogel, B. Wiering, T. J. Ruers, N. Karssemeijer, and W. J. Oyen, "A novel iterative method for lesion delineation and volumetric quantification with FDG PET," Nucl. Med. Commun. **28**, 485–493 (2007).

[24] W. Jentzen, L. Freudenberg, E. G. Eising, M. Heinze, W. Brandau, and A. Bockisch, "Segmentation of PET volumes by iterative image thresholding," J. Nucl. Med. **48**, 108–114 (2007).

[25] J. Weickert, Anisotropic Diffusion in Image Processing (B. G. Teubner Stuttgart, Stuttgart, Germany, 1998).

[26] P. Perona and J. Malik, "Scale-space and edge detection using anisotropic diffusion," IEEE Trans. Pattern Anal. Mach. Intell. **12**, 629–639 (1990).

[27] J. F. Canny, "A computational approach to edge detection," IEEE Trans. Pattern Anal. Mach. Intell. **8**, 679–698 (1986).

[28] M. N. Do and M. Vetterli, "The contourlet transform: an efficient directional multiresolution image representation," IEEE Trans. Image Process. **14**, 2091–2106 (2005).

[29] S. Mallat, A Wavelet Tour of Signal Processing, Third Edition: The Sparse Way (Academic, New York, 2008).

[30] W. R. Boukabou and A. Bouridane, "Contourlet-based feature extraction with PCA for face recognition," in Proceedings of the NASA/ESA Conference on Adaptive Hardware and Systems (AHS '08), Noordwijk (IEEE, 2008), pp. 482–486.

[31] P. J. Burt and E. H. Adelson, "The Laplacian pyramid as a compact image code," IEEE Trans. Commun. **31**, 532–540 (1983).

[32] R. H. Bamberger and M. J. T. Smith, "A filter bank for the directional decomposition of images: theory and design," IEEE Trans. Image Process. **40**, 882–893 (1992).

[33] Z. Hong-Kai, T. Chan, B. Merriman, and S. Osher, "A variational level set approach to multiphase motion," J. Comput. Phys. **127**, 179–195 (1996).

[34] W. P. Segars, G. Sturgeon, S. Mendonca, J. Grimes, and B. M. Tsui, "4D XCAT phantom for multimodality imaging research," Med. Phys. **37**, 4902–4915 (2010).

[35]A. Le Maitre, W. P. Segars, S. Marache, A. Reilhac, M. Hatt, S. Tomei, C. Lartizien, and D. Visvikis, "Incorporating patient specific variability in the simulation of realistic whole body 18F-FDG distributions for oncology applications," Proc. IEEE 97, 2026–2038 (2009).

[36]K. Thielemans, C. Tsoumpas, S. Mustafovic, T. Beisel, P. Aguiar, N. Dikaios, and M. W. Jacobson, "STIR: Software for tomographic image reconstruction release 2," Phys. Med. Biol. 57, 867–883 (2012).

[37]X. Geets, J. Lee, A. Bol, M. Lonneux, and V. Gregoire, "A gradient-based method for segmenting FDG-PET images: Methodology and validation," Eur. J. Nucl. Med. Mol. Imaging 34, 1427–1438 (2007).

[38]M. Wanet, J. A. Lee, B. Weynand, M. De Bast, A. Poncelet, V. Lacroix, E. Coche, V. Gregoire, and X. Geets, "Gradient-based delineation of the primary GTV on FDG-PET in non-small cell lung cancer: A comparison with threshold-based approaches, CT and surgical specimens," Radiother. Oncol. 98, 117–125 (2011).

[39]T. Shepherd, M. Teras, R. R. Beichel, R. Boellaard, M. Bruynooghe, V. Dicken, M. J. Gooding, P. J. Julyan, J. A. Lee, S. Lefevre, M. Mix, V. Naranjo, X. Wu, H. Zaidi, Z. Zeng, and H. Minn, "Comparative study with new accuracy metrics for target volume contouring in PET image guided radiation therapy," IEEE Trans. Med. Imaging 31, 2006–2024 (2012).

[40]T. Shepherd, B. Berthon, P. Galavis, E. Spezi, A. Apte, J. A. Lee, D. Visvikis, M. Hatt, E. de Bernardi, S. Das, I. El Naqa, U. Nestle, C. R. Schmidtlein, H. Zaidi, and A. Kirov, "Design of a benchmark platform for evaluating PET-based contouring accuracy in oncology applications [abstract]," Eur. J. Nucl. Med. Mol. Imaging 39, S264 (2012).

[41]J. Bezdek, R. Hathaway, M. Sobin, and W. Tucker, "Convergence theory for fuzzy c-means: Counterexamples and repairs," IEEE Trans. Syst. Man Cybern. 17, 873–877 (1987).

[42]M. Hatt, F. Lamare, N. Boussion, A. Turzo, C. Collet, F. Salzenstein, C. Roux, P. Jarritt, K. Carson, C. Cheze-Le Rest, and D. Visvikis, "Fuzzy hidden Markov chains segmentation for volume determination and quantitation in PET," Phys. Med. Biol. 52, 3467–3491 (2007).